Preprints are preliminary reports that have not undergone peer review.
They should not be considered conclusive, used to inform clinical practice,
or referenced by the media as validated information.

Preparation and characterization of nanocomposite thin films containing gold nanoparticles by single-step atmospheric pressure plasma deposition process

Elène Bizeray
Université de Toulouse
Antoine Belinger
Université de Toulouse
Simon Dap
Université de Toulouse
Sophie Nowak
Université Paris Cité, France
Philippe Decorse
Université Paris Cité, France
Souad Ammar
Université Paris Cité, France
Fiorenza Fanelli
National Research Council
Nicolas Naudé
naude@laplace.univ-tlse.fr

Université de Toulouse

Research Article

Keywords: Dielectric Barrier Discharge, nanocomposite, metal salts, PECVD, aerosol

Posted Date: December 17th, 2025

DOI: https://doi.org/10.21203/rs.3.rs-8223792/v1

License: 🅭 🅯 This work is licensed under a Creative Commons Attribution 4.0 International License.
Read Full License

Additional Declarations: No competing interests reported.

Preparation and characterization of nanocomposite thin films containing gold nanoparticles by single-step atmospheric pressure plasma deposition process

Authors:

Elène Bizeray[1], Antoine Belinger[1], Simon Dap[1], Sophie Nowak[2], Philippe Decorse[2], Souad Ammar[2], Fiorenza Fanelli[3]* and Nicolas Naudé[1]*

[1] Univ Toulouse, Toulouse INP, CNRS, Laplace, Toulouse, France

[2] Université Paris Cité, CNRS, ITODYS, Paris, France

[3] National Research Council (CNR), Institute of Chemistry of Organometallic Compounds (ICCOM), Bari Secondary Unit, Bari, Italy

Corresponding authors: fiorenza.fanelli@cnr.it, naude@laplace.univ-tlse.fr

Abstract

This study focuses on the plasma deposition of metal/polymer nanocomposite thin films at atmospheric pressure and low temperature. The synthesis process combines a dielectric barrier discharge (DBD) with an aerosol of a solution of a gold salt (*i.e.*, tetrachloroauric acid trihydrate, $HAuCl_4 \cdot 3H_2O$) in isopropanol. In particular, the solution is injected as an aerosol into a parallel-plate DBD fed with nitrogen and powered by a dual-frequency modulated (800 Hz/20 kHz) sinusoidal high voltage. The influence of duty cycle variation (*i.e.*, the ratio of high-frequency time to total cycle time) on the properties of the deposited layers is assessed, keeping constant the gold salt concentration in the aerosolized solution. The chemical composition, morphology, and optical properties of the deposited layers are determined using various characterization techniques, including attenuated total reflectance-Fourier transform infrared spectroscopy, X-ray photoelectron spectroscopy, X-ray diffraction, UV-Visible absorption spectroscopy, and scanning electron microscopy with energy dispersive X-ray spectrometry. It appears that increasing the duty cycle affects both the growth rate of the nanocomposite thin film and the efficiency in gold salt reduction into metallic nanoparticles, thereby influencing the plasmonic properties. Overall, these results offer new insights into the potential of using a single-step aerosol-assisted plasma process to deposit functional organic/inorganic nanocomposite thin films at atmospheric pressure.

Keywords: Dielectric Barrier Discharge, nanocomposite, metal salts, PECVD, aerosol

I. Introduction

In recent years, nanocomposite (NC) thin films have demonstrated their potential in different application fields (for example, improvement of the efficiency of photovoltaic panels [1, 2], optoelectronics [3], and anti-microbial properties of surfaces [4], among others). These NCs typically consist of an organic matrix incorporating inorganic fillers of nanoscale dimension [5].

Over the last few decades, plasma processes, such as plasma-enhanced chemical vapor deposition (PECVD), have proven to be very useful for NC thin film deposition [6]. PECVD generally operates at low pressure, but despite its efficiency, there is still a growing need for low-cost and large-scale deposition techniques. Therefore, a process at atmospheric pressure could be an interesting alternative. However, working at such a pressure requires careful control of plasma to prevent gas thermalization. To achieve this, a robust solution is the use of dielectric barrier discharge (DBD). DBD is already widely deployed, in particular for surface functionalization and for the deposition of polymeric or inorganic thin films [7–9]. Attention has only recently been focused on the use of DBDs for NC thin film deposition [10].

At atmospheric pressure, plasma processes are easily compatible with aerosol injection, offering great flexibility in the choice of precursors and facilitating their delivery to the deposition zone [11]. For the deposition of organic/inorganic NC thin films, dispersions of preformed inorganic nanoparticles (NPs) in a suitable organic solvent are typically used [12]. The solvent generates an aerosol of microdroplets that encapsulate and transport the NPs. These droplets act as carriers toward the plasma region, where the solvent dissociates, enabling controlled matrix growth. The tendency of NPs to agglomerate in aerosol droplets due to solvent evaporation can be a drawback for the production of homogeneous NC films [13]. Therefore, some ligands or surfactants are often grafted on the NP surface to limit such a phenomenon, adding supplementary preparative steps [14, 15]. Nadal *et al.* [16] recently proposed an alternative, replacing NP dispersions in an organic solvent with metallic salt solutions, the solvent undergoing plasma polymerization, while the cations undergoing chemical reduction. In practice, Nadal *et al.* combined a DBD in argon atmosphere with the aerosol of an isopropanol solution of a gold salt (*i.e.*, tetrachloroauric acid (III) trihydrate, $HAuCl_4 \cdot 3H_2O$). They used a Frequency Shift Keying (FSK) modulation signal that alternates between high-frequency (HF) and low-frequency (LF) phases (20 kHz and 800 Hz, respectively [16]). As the HF phase is more powerful, it provides the energy needed to reduce the gold salt to metal NPs, while allowing the matrix to grow by dissociation of the precursor, followed by polymerization. Reversely, LF excitation phase ensures NPs transport and deposition on the substrate surface [17]. Besides, modifying deposition parameters, such as the duration of the HF phase over the total cycle duration, gold concentration, or FSK frequency, allows modulating the properties of the resulting NC films, especially the average metal NP size and the substrate surface coverage rate.

Perdrau *et al.* then continued this work by changing the plasma carrier gas from argon to argon/ammonia mixture [18], and superposing the HF and LF voltages. Based on Bazinette *et al.* work, which evidenced that the application of the LF voltage does not affect the HF phase [19], Pedrau et al., applied the HF phase for 2.5 ms, every 10 ms [18]. They highlighted the fact that ammonia addition leads to NH_4AuCl_4 precipitation, blocking gold cation reduction [18].

Bjelajac et al. [19] and Vasudevan et al. [20] investigated the use of $HAuCl_4 \cdot 3H_2O$ dissolved in ethanol as a precursor in argon plasma jets, injecting the alcoholic solution directly into the plasma rather than into the post-discharge region, and succeeded in producing gold NPs.

Overall, previous publications demonstrated the proof-of-concept of this innovative deposition strategy using an Ar DBD and Ar plasma jet. However, only a few characterization techniques were employed to assess the properties of the produced thin film. Published works mainly focused on the plasma properties and the morphology of the deposit using mainly UV-Visible absorption spectroscopy and atomic force microscopy (AFM) or scanning electron microscopy (SEM). Chemical and structural analyses, using , for instance, attenuated total reflectance-Fourier transform infrared spectroscopy (ATR-FTIR), X-ray photoelectron spectroscopy (XPS) and X-ray diffraction (XRD), are often missing.

One of the main aims of this work is therefore to deeply characterize the produced NC deposits, to understand the role of the different operating parameters on both the polymeric matrix growth and the gold salt reduction, employing a large set of techniques. UV-Visible absorption spectroscopy was used to confirm the presence of gold NPs and to obtain information on their size distribution as well as their surrounding environment, but also ATR-FTIR, XPS, XRD and

SEM were also used to have an overview of the overall chemical composition, structure and morphology of the deposits.

Besides, to the best of our knowledge, nitrogen was never tested as carrier gas in such plasma-based deposition process. Although nitrogen is significantly less expensive than argon, its molecular structure makes it more difficult to initiate discharge. For the same pressure × distance product, the breakdown voltage required in nitrogen is higher, and then more intense electric fields are needed to initiate the discharge. At the same time, So high electric fields may affect precursor dissociation and matrix growth. As a consequence, another aim of this work is to study the influence of duty cycle variation (*i.e.*, the ratio of HF phase time to total cycle duration) on the properties of the deposited NC thin films for a selected gold salt concentration in the atomized solution, using nitrogen as carrier gas.

II. Experimental section

II.1. Atmospheric pressure PECVD experimental setup

Fig. 1 illustrates the experimental setup used for the deposition of NC thin films. It consists of two main parts: the vessel containing the discharge cell for thin film deposition and the aerosol generator system.

The discharge cell is located inside a vessel described in a previous publication [20]. It presents a DBD configuration with a 1 mm gas gap. Two parallel silver electrodes with a rectangular surface area, defined by a width of 3 cm and a length of 3.35 cm, are used. Each electrode is covered by a 0.635 mm thick Al_2O_3 dielectric plate. The gas and precursor solution are injected between the two dielectrics and guided by two glass or quartz bars until the gas exits on the opposite side. This ensures a laminar gas flow in the discharge region.

The pressure is controlled and maintained at 1000 mbar during the process by using a solenoid valve connected to a diaphragm pump and a pressure control system.

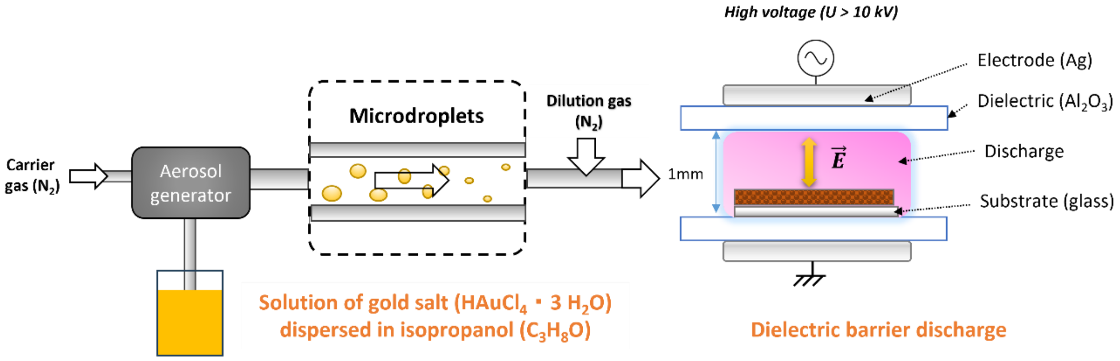

Fig. 1 Global view of the experimental setup used for NC film deposition

During the deposition process, the precursor solution is injected into the plasma as an aerosol. The solution consists of a gold salt ($HAuCl_4{\cdot}3H_2O$, 99.99% purity, Aldrich) dissolved in isopropanol (C_3H_8O, 99.98% purity, Aldrich) with 0.3 wt% Au (which is the percentage of gold mass in the mixture). Aerosol generation is achieved using a constant output atomizer purchased from TSI (*TSI 3076)*. This aerosol was recently characterized by *Perdrau et al.* [18]. The differential mobility analyses showed that the size of the produced droplets drastically reduces in a few hundred milliseconds after aerosol generation due to the fast evaporation of the solvent [21]. According to their study, the modal diameter of the droplets entering in the discharge cell is around 25-30 nm. A nitrogen flow rate of 1.1 slm is supplied to the atomizer to generate a stable and continuous aerosol. Under these operating conditions, the atomizer delivers solution flow rates of 148 ± 5 mg/min. To control the precursor concentration in the discharge, the aerosol is diluted with a 2 slm nitrogen flow rate. It follows that the mean gas residence time in the discharge region during the deposition experiments is equal to 20 ms .

To control the matrix formation and NP transport to the surface separately, a double excitation frequency is used. For this purpose, a waveform with the desired shape is generated by using a programmable function generator (HMF2525, 25 MHz *Rhode & Schwarz)*. An example of a typical dual excitation frequency signal is illustrated in Fig. 2. This function generator can also modulate the time spent at each frequency or adjust the amplitude of one signal in relation to another, among other features. The generated waveform is supplied to an audio amplifier (1800 W in a 4 Ω load, *Crest Audio CA18*), whose output is then connected in series with the primary winding of a high-voltage transformer (600 VA, 60V/9kV, *Montoux*). The secondary winding is connected to the discharge cell, in series with a shunt resistor to measure the current. A high-voltage probe (*Tektronix* P6015A) is also used to measure the voltage at the transformer output.

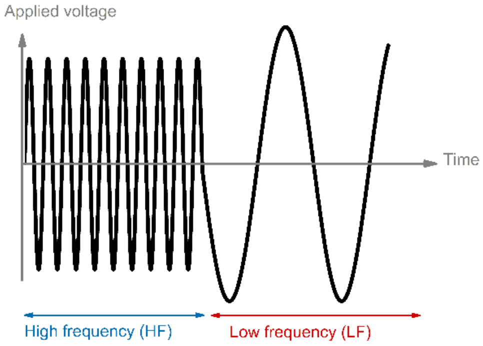

Fig. 2 Example of the double frequency excitation signal used in the deposition process

From the application duration of the HF and LF phases, it is possible to determine the duty cycle (DC) value, defined as $DC = t_{HF}/t_{cycle}$ where t_{HF} corresponds to the time spent at high frequency and t_{cycle} to the total cycle duration. The higher the DC, the longer the duration of the HF phase. As the gas residence time is 20 ms in the typical conditions of the deposition process, the total cycle duration is set at 40 ms, to give the gas molecules time to cross and fill the entire discharge zone. In this way, at a DC of 0.5 (*i.e.* 20 ms at HF and 20 ms at LF), the space can be filled for both excitation frequencies. This makes it possible to appreciate the effect of the DC variation.

The aerosol injection has an influence on the discharge behavior. Due to the high injected amount of precursor, a filamentary regime is always observed in this work, with a power close to 2.3 W/cm² and to 0.1 W/cm² at HF and LF phases, respectively. As DC increases, the average discharge energy increases. It is worth mentioning that, synthetizing uniform thin films with this regime can be challenging due to the localized energy injection [22].

The deposition is performed for 10 min on a rectangular glass substrate (size of 48 x 64 mm, thickness of 0.2 mm) placed on the alumina plate covering the ground electrode. Table 1 summarizes all the experimental conditions used to perform the deposition of NC thin films.

Table 1 Experimental conditions used for NC film deposition

Sample name		**S1**	**S2**	**S3**	**S4**	**S5**
Aerosol inlet gas flow rate		1.1 slm				
Aerosol mass flow rate		148 ± 5 mg/min				
Dilution gas flow rate		2 slm				
Duty cycle		1	0.75	0.5	0.25	0
Low frequency phase	Frequency	No LF	800 Hz			
	Discharge power		$P_{LF} = 0.1 \pm 0.02$ W/cm²			
	Duration of application		10 ms	20 ms	30 ms	40 ms
High frequency phase	Frequency	20 kHz				No HF
	Discharge power	$P_{HF} = 2.3 \pm 0.05$ W/cm²				
	Duration of application	40 ms	30 ms	20 ms	10 ms	
Deposition process duration		10 min				

II.2. Nanocomposite films characterization

The chemical composition, morphology and optical properties of the produced NC thin films are determined by using various characterization techniques. Three measurements are taken per sample along the direction of the gas flow. Indeed, for each sample, three distinct positions along the gas flow direction have been considered for all the analyses, except for XRD, to assess the effect of residence time in the discharge region. In the case of XRD, a single analysis is performed per sample due to the large size of the X-ray spot on the sample surface (~2 cm).

Stylus profilometry is used to determine the thickness of the deposited coatings. Before measurement, the coating is scratched in the different zones of characterization, by using a stainless-steel tweezer. Measurements are made by applying a low strength on the stylus tip, to ensure accurate thickness determination.

UV-VIS absorption spectra are acquired on a 1 mm spot using a *Thorlabs SLS201L/M* tungsten/halogen lamp to cover the UV-Vis range. A spectrometer from *Get Spec* (Get Spec 2048 TEC) is employed for spectra acquisition over a large range of wavelength with a resolution of 0.6 nm.

XRD patterns are recorded on a *Panalytical* Xpert'Pro diffractometer equipped with a cobalt X-Ray radiation source (1.7889 Å), operating in a θ-θ reflexion Bragg Brentano configuration. The patterns are analyzed by Highscore+ software version 3.5.0 (PANALYTICAL®).

SEM micrographs are collected on the samples using a *Jeol* 7800F Prime microscope, operating at 10 kV. An Everhart-Thornley detector is used to visualize the general topography of the deposits at low magnification and to evaluate the surface coverage. A backscattered electron detector is used to acquire images emphasizing atomic number contrast. Before SEM observations, samples are metalized with a 5 nm chromium layer. The employed microscope is also equipped with an Energy Dispersive X-ray spectrometer (EDS) allowing elemental chemical analysis.

To complete chemical characterization, ATR-FTIR spectra are acquired by using a *VERTEX 70* spectrophotometer from *Bruker* with a Germanium ATR crystal. XPS analyses are performed using a Thermo VG ESCALAB 250 instrument equipped with a microfocused, monochromatic Al-K_α X-ray source (1486.6 eV) and a magnetic lens. Broad and narrow scans are acquired in a constant analyzer energy mode with pass energies of 150 and 40 eV, respectively. The binding energy scale is referenced to the hydrocarbon component of the C1s spectrum at 284.8 ± 0.2 eV. The data are analysed using Advantage software version 5.9902 (THERMO-FISHER®).

III. Results and discussion

III.1. Visual appearance of the deposited NC films and thickness measurements

Fig. 3 shows the pictures of the samples taken immediately after film deposition using different DC values. All samples are photographed from the same angle, with the same brightness and the same settings, in order to compare their appearance.

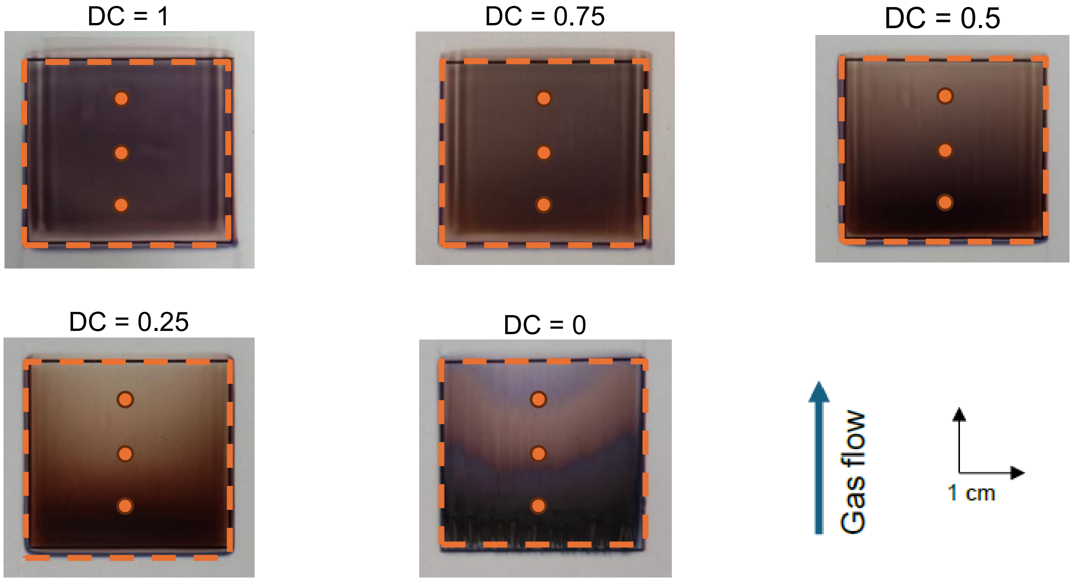

Fig. 3 Photographs of the synthesized NC films as a function of DC. The electrode boundary is indicated by the black rectangle surrounding each deposit. The blue arrow indicates the direction of the gas flow. The orange circles indicate the location where the characterizations are carried out

It is interesting to note that the color of the coatings differs depending on DC value. Indeed, for samples deposited with a high proportion of HF excitation (DC = 1 and DC = 0.75), the color is rather violet, and the films appear homogeneous, whatever the position on the substrate. However, for DC = 0.25 and DC = 0.5, the deposits exhibit a color tone in the brown range, with a darker zone at the entrance that varies according to the operating conditions. When the proportion of HF excitation is higher (DC = 0.5), the dark zone appears to extend over a longer distance. This could be ascribed to the fact that the formed gold particles are trapped for a longer period of time in the gas gap and are therefore deposited further onto the sample surface. With LF excitation only (DC = 0), the sample has a significantly different appearance because the film deposition does not start right immediately at the beginning of the discharge zone. This could be explained by the fact that the energy per precursor molecule is relatively low at this frequency range. It takes longer time to dissociate the precursor and deposit the film. Also the color of this sample evolves a lot along the gas flow direction, likely due to the poor matrix synthesis.

Thickness measurements provide insight into how DC influences the matrix synthesis and the incorporation of gold NPs in it. Table 2 shows the thin film thickness values for each deposition conditions at the three different measurement zones for each sample.

Table 2 Mean thicknesses values measured on the NC deposits using different values of DC (relative standard deviation of 20%)

	Entrance	Center	Exit
DC = 1	≈ 540 nm	≈ 610 nm	≈ 650 nm
DC = 0.75	≈ 580 nm	≈ 600 nm	≈ 620 nm
DC = 0.5	≈ 460 nm	≈ 500 nm	≈ 610 nm
DC = 0.25	Not measurable		
DC = 0			

For DC = 1, the coating thickness increases progressively with position along the substrate. For a DC = 0.75, the thickness remains nearly constant, showing little dependence on position or residence time. In contrast, at DC = 0.5 a much stronger increase is observed, with the thickness rising by about 150 nm from the entrance to the exit of the substrate. Overall, thickness slightly increases as the HF proportion increases, which could suggest an enhancement of the isopropanol polymerization by the HF excitation.

The thin films deposited at DC = 0 and DC = 0.25 have a more viscous appearance, which is consistent with the fact that no thickness measurements can be made on these samples by profilometry. Indeed, the tip of the profilometer's stylus scratches the coating, and the measurement is therefore not accurate. For these two samples, the mean injected power density is too low (Table 1), which has a substantial impact on the dissociation of the NC matrix precursors (i.e., isopropanol) [9].

III.2. Optical characterization of the produced NC films

UV-Vis absorption spectroscopy is a useful technique for characterizing gold NPs. Indeed, the irradiation of gold NPs with an electromagnetic wave excites the exposed medium, which will set the electrons in motion and create a dynamic polarization, leading to light absorption in the visible range (plasmonic band). The charge oscillation varies according to particle size, shape, distance between particles, and other factors [23, 24], and the related band absorption position and intensity change consequently. So, if gold NPs are present in the plasma-deposited films an absorption band in the visible region must be evidenced in the recorded spectra. Fig. 4 reports the UV-Vis absorption spectra of the samples prepared with different DC values. It is worth mentioning that they are not normalized by the thickness, because coatings with DC < 0.5 are too soft for thickness measurements.

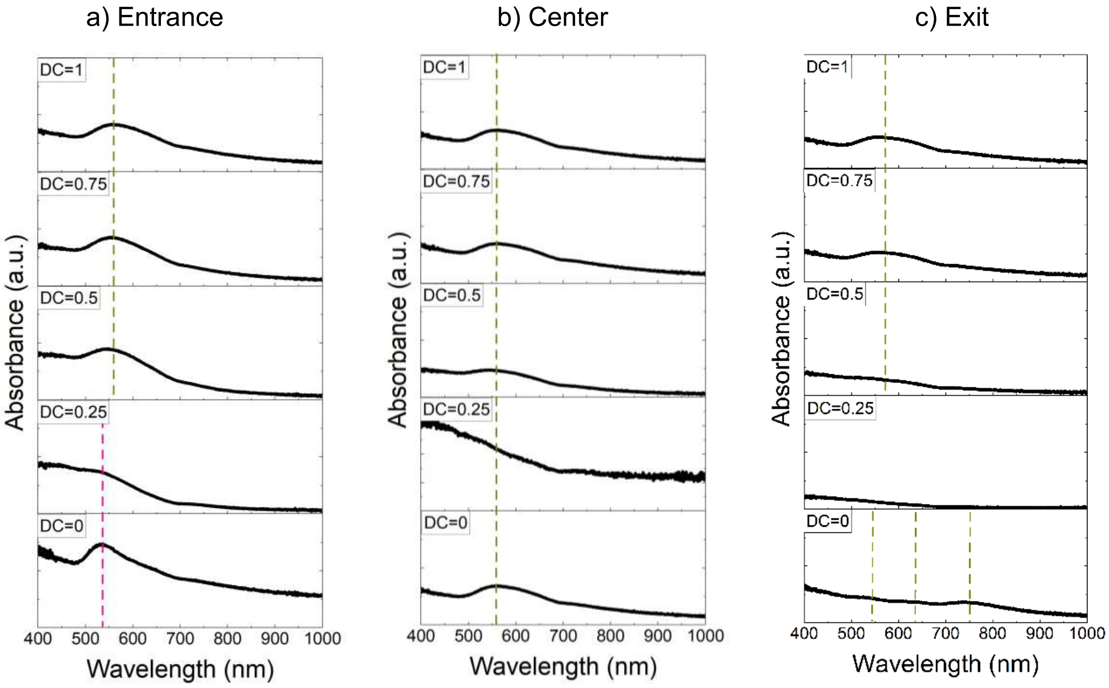

Fig. 4 UV-Vis absorption spectra of the synthesized sample as a function of DC. Each graph corresponds to the measurement on the different sample positions: **a** the entrance, **b** the center, and **c** the exit

At the entrance position (Fig. 4a), there are two different plasmonic responses. For DC ≥ 0.5, the plasmonic band is centered at 560 nm, whereas for the other samples, it is centered at 530 nm. The shift to higher wavelengths could be explained by the viscosity of the polymer matrix deposited at lower DC and/or by an increase of the average dimension of the Au NPs as a function of DC. The spectra also evidence a weak contribution at 720 nm due to the presence of larger size NP population.

At the center position (Figure 4b), the main plasmonic band centered at 560 nm and the small contribution at 720 nm are always observed.

At the exit position (Figure 4c), for the sample produced at DC = 0, several plasmonic bands with maxima at 540, 640, and 750 nm are observed, as a consequence of gold NP size distribution. For the sample produced at DC = 0.25, no plasmonic response is visible, indicating that either the quantity of gold present in the layer is less significant or it is high but associated with strongly aggregated gold NPs [25]. For the samples obtained at higher DC values, the plasmonic band centered at 530 nm becomes increasingly visible with the increase in DC. Overall, plasmonic responses appear to be similar across samples regions (i.e. residence times) at high DC (≥ 0.75), which is consistent with the hypothesis that NPs are trapped longer in the gas phase and can deposit further out on the substrate [16].

III.1. Chemical composition of the produced NC films

III.1.a. ATR-FTIR

Fig. 5 shows the ATR-FTIR spectra, recorded on the samples prepared at different DC values, for the entrance, center, and exit positions. The peak assignment is presented in Table 3.

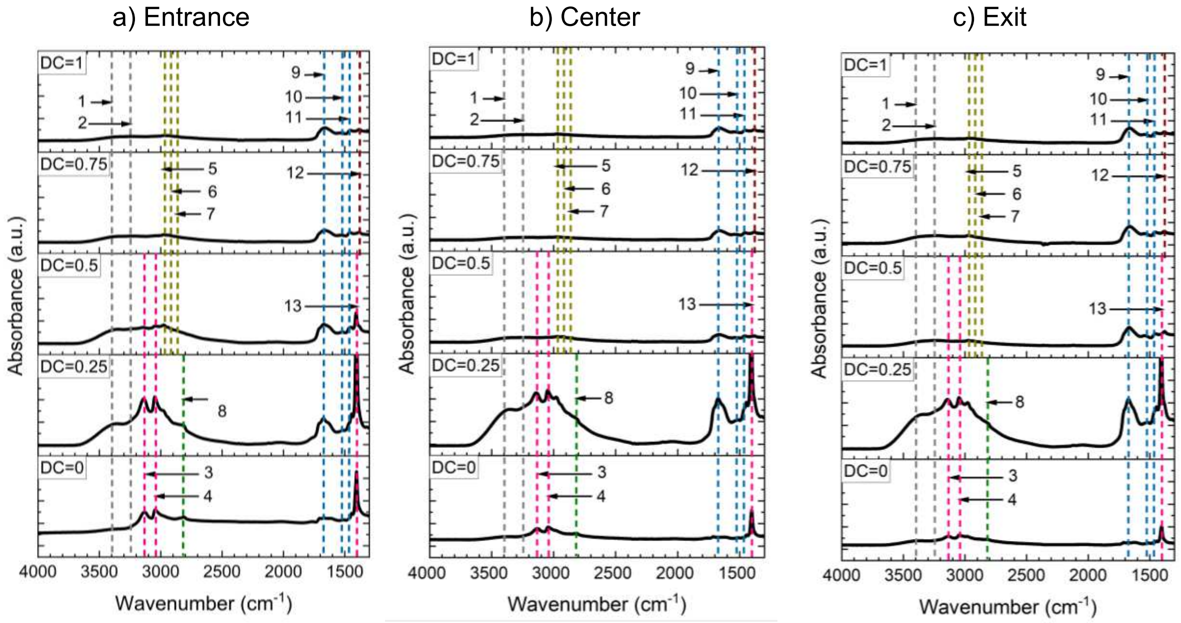

Fig. 5 ATR-FTIR spectra of the NC films deposited at different DC values. Spectra are collected at **a** the entrance, **b** the center, and **c** the exit positions on each sample. Peak assignments are summarized in Table 3

Table 3 FTIR peak assignments for the NC films deposited at different DC values

Peak	Wavenumber (cm^{-1})	Assignment [26–28]
1	3370	OH stretching
2	3220	NH stretching in amino groups (NH_x)
3	3120	NH stretching in NH_4^+
4	3040	
5	2980	CH_x sp^2/sp^3 stretching
6	2930	
7	2860	
8	2800	Overtone of NH bending in NH_4^+
9	1640	C=O or C=C stretching
10	1510	NH bending in amino groups (NH_x)
11	1450	CH_x sp^2/sp^3 bending
12	1380	
13	1400	NH bending in NH_4^+

All ATR-FTIR spectra present the absorption peaks of a carbon-based matrix with sp^3 and sp^2 CH_x groups (CH_x stretching between 2860 and 3280 cm^{-1}, CH_x bending between 1370 and 1450 cm^{-1}) as well as carbonyl (C=O stretching at 1640 cm^{-1}) and hydroxyl (OH stretching at 3370 cm^{-1}) functionalities. In addition, all samples show the incorporation of nitrogen in the form of amine groups (NH stretching at 3220 cm^{-1} and NH bending at 1510 cm^{-1}). It is worth specifying that the formation of nitrogen-containing functionalities is due to the dissociation of nitrogen and isopropanol molecules in the plasma, and subsequent recombination reactions.

Fig. 5 shows that the whole spectra shape depends on DC values. Indeed, when the proportion of LF excitation is high (DC < 0.5), typical absorptions related to ammonium (NH_4^+) appear [28], whatever the position on the substrate (typical peaks of NH stretching and NH bending at of 3040-3120 cm^{-1} and 1400 cm^{-1} respectively). For DC = 0.5, ammonium absorption peaks are identified only at the entrance and barely in the center. The amplitude of the NH_4^+ peaks is inversely proportional to the time spent at HF, which raises the question on why the formation of ammonium ion occurs when the ratio of discharge energy per precursor molecule is low.

III.1.b. XPS

Table 4 summarizes the surface chemical composition determined by XPS at the entrance, center, and exit positions for all produced samples with various DC values. Interestingly, no appreciable variation in the surface atomic percentages with the positions is observed. These percentages are representative of the uppermost 10 nm of the deposits. Silicon (not shown in the Table 4) is only detected at very low concentration (< 1%) at the exit of the sample deposited at DC = 1, meaning except this case, the glass substrate are fully covered. It is not excluded that this silicon signature can come from the proximity of the measurement position, in this sample, with the glass splinter coming from sample cutting.

Table 4 Surface atomic concentrations determined by XPS for various DC values at the entrance, the center and the exit positions of each sample

	Position	C (at%)	O (at%)	N (at%)	Au (at%)	Cl (at%)
DC = 1	Entrance	71±4	11.0±0.5	14.0±0.6	0.10±0.01	4.0±0.2
	Center	71±4	11.0±0.5	14.0±0.7	0.10±0.01	4.0±0.2
	Exit	71±4	11.0±0.5	14.0±0.7	< 0.1	4.0±0.2
DC = 0.75	Entrance	68±3	11.0±0.5	15.0±0.7	0.10±0.01	5.0±0.2
	Center	68±3	11.0±0.5	16.0±0.8	0.10±0.01	5.0±0.2
	Exit	68±3	11.0±0.5	15.0±0.7	< 0.1	5.0±0.3
DC = 0.5	Entrance	67±3	12.0±0.5	15.0±0.7	0.10±0.01	5.0±0.3
	Center	67±3	12.0±0.5	15.0±0.7	< 0.1	6.0±0.3
	Exit	67±3	13.0±0.6	15.0±0.7	< 0.1	5.0±0.3
DC = 0.25	Entrance	65±3	12.0±0.5	16.0±0.8	0.40±0.04	7.0±0.4
	Center	65±3	12.0±0.5	16.0±0.8	0.10±0.01	7.0±0.4
	Exit	65±3	13.0±0.6	16.0±0.8	0.10±0.01	6.0±0.3
DC = 0	Entrance	60±3	14.0±0.7	14.0±0.7	6.0±0.6	5.0±0.3
	Center	63±3	13.0±0.6	14.0±0.7	3.0±0.3	7.0±0.4
	Exit	64±3	12.0±0.5	14.0±0.7	1.0±0.1	7.0±0.4

Second, for the carbon concentration, a slight decrease in the surface concentration from about 72 at% to about 60 at% is observed with decreasing the DC value. In contrast, the gold concentration presents a specific behavior. Indeed, for DC ≥ 0.5, the amount of gold is always very low (close to 0.1 at%). Given the measurement uncertainty and the low values detected, no clear correlation can be established between the variation of these percentages and either the DC value or the measurement position. Nevertheless, one may say that by lowering DC, the amount of gold increases, up to reaching a few atomic percentages for DC = 0. Also, the Au surface atomic concentration of the coating decreases with increasing the residence time.

The deconvolution of the high resolution Au4f XPS spectra is presented in Fig. 6. It was performed with the help of the NIST database [29] and of the specific literature [30,31] dealing with gold oxidation state determination by XPS. In the present study, all the spectra are modeled with the spin–orbit doublet (4f$_{7/2}$ and 4f$_{5/2}$) for each gold component (Au^0 and/or Au^{3+}). and the Shirley background. The Au4f$_{7/2}$ and Au4f$_{5/2}$ components of each spin–orbit doublet are generally separated by 3.7 eV, with 4f$_{7/2}$ binding energy of 84 eV and 85 eV (± 0.2 eV) for Au^0 and Au$^+$, respectively. Sometimes there are slightly binding energy shifts for the same chemical group that could be observed. Bjelajac *et al.* demonstrated that these shifts could be attributed to the presence of polymer surrounding the NPs, which varies depending on the experimental conditions [32].

It is essential to note that for DC < 0.5, the salt is completely reduced regardless of the position, since only the presence of metallic gold (Au^0) is revealed in the recorded spectra. For DC =

0.5, only Au^0 is evidenced at the entrance, while a mixture of Au$^+$ and Au^0 are observed at the center and at the exit of the sample. For DC > 0.5, partially (Au$^+$) and totally (Au^0) reduced gold are simultaneously detected in all the samples whatever the substrate position. Finally, the higher the DC, the greater the proportion of Au$^+$ found, suggesting a deposition of the salt on the sample surface and its encapsulation in the organic matrix before its total reduction.

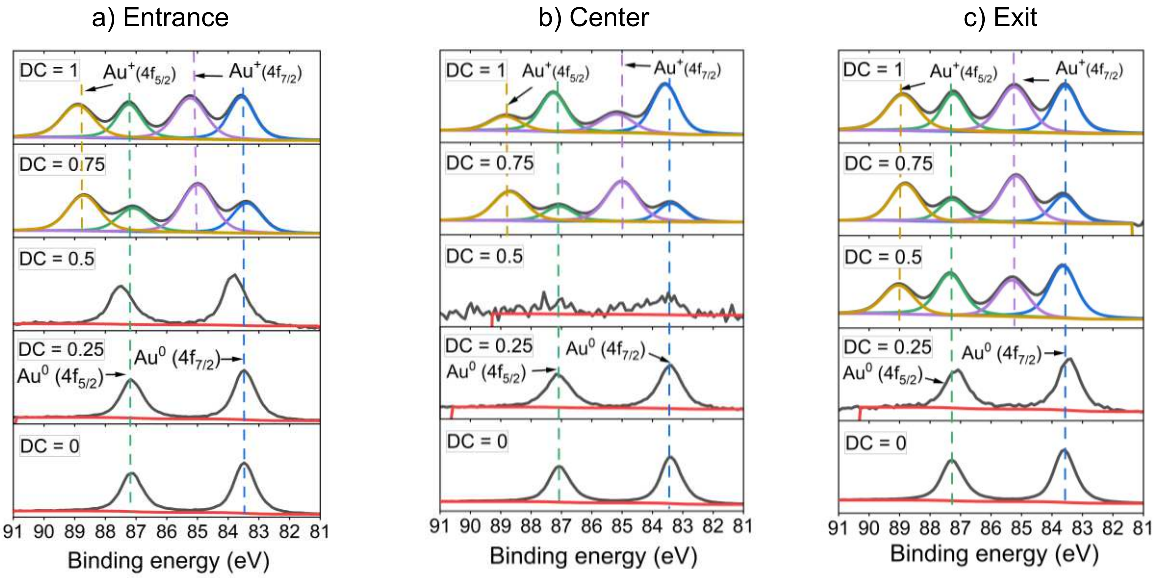

Fig. 6 High resolution XPS spectra of the Au4f signal measured at the **a** entrance, **b** center and **c** exit positions of all the produced NC films for different DC values. The red line indicates the background signal (baseline)

Compared to Au4f XPS signal, those of C1s, O1s, N1s and Cl2p appear to be less affected by the DC value and the analysis position on the samples. The deconvolution of the high-resolution C1s, O1s, N1s and Cl2p XPS spectra at the entrance of samples deposited at DC = 0, 0.5 and 1 are presented in Fig. 7. It is essential to note that these peaks do not change with the gas residence time. The attributions of the components of the different high-resolution XPS spectra are based on Thermofisher [33] and NIST databases [29].

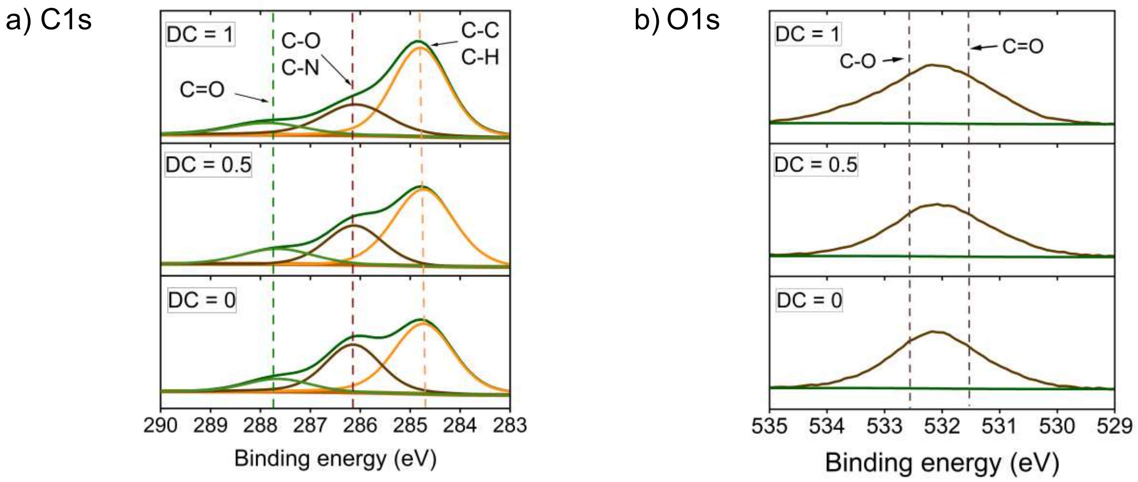

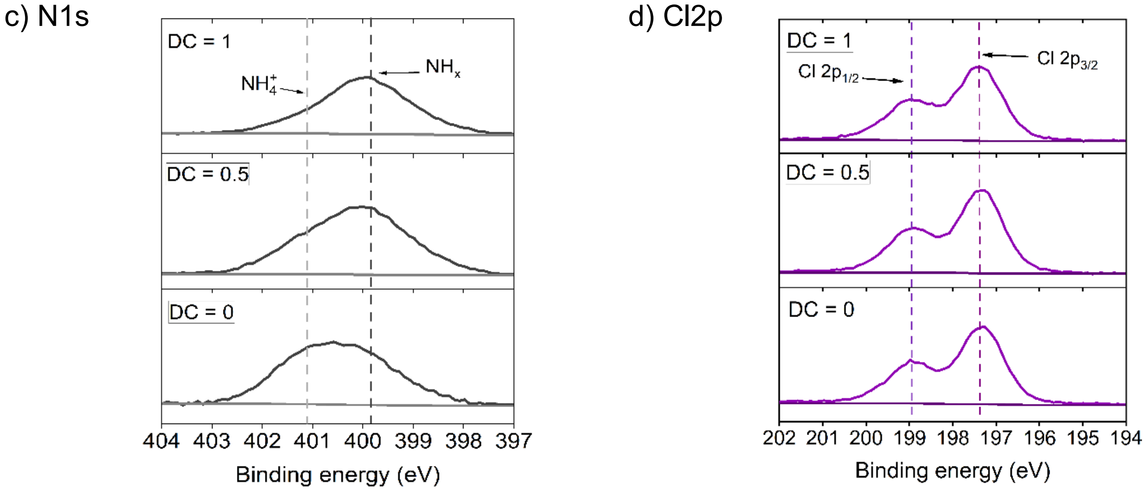

Fig. 7 High resolution (a)C1s, (b) O1s, (c) N1s, (d) Cl2p XPS spectra at the entrance of the samples deposited at DC = 0, DC = 0.5 and DC = 1

The high-resolution C1s XPS spectrum (Fig. 7a) was curve-fitted with three peaks, centered at binding energies of 284.8, 286.2 and 287.6 eV, and ascribed to C-H/C-C (alkane and alkene), C-O/C-N and C=O groups, respectively. The relative contribution of these components remains relatively constant as a function of DC.

The O1s spectrum (Fig. 7b) showed a large peak centered at 532 eV, which can include contributions from both O-C and O=C groups typically found at approximately 532.5 eV and 531.5 eV.

The N1s signal (Fig. 7c) presents two contributions at 399.8 eV and 401.3 eV, consistent with the presence of amino and ammonium groups. Here, the amplitude of the ammonium ion peak increases with time spent at low frequency (i.e., by decreasing the DC value).

The Cl2p signal (Fig. 7d) is typical of that of chloride salt (Cl2p$_{3/2}$ peak at 197.6 eV [34]), as it can match with the signature of ammonium chloride [29].

III.1.c. XRD

The collected XRD patterns for the different DC values are presented in Fig. 8. They are analyzed by comparing the observed peak positions with those of tabulated patterns for gold (ICDD 98-004-4362, PDF2) and ammonium chloride (ICDD 98-002-0682, PDF2).

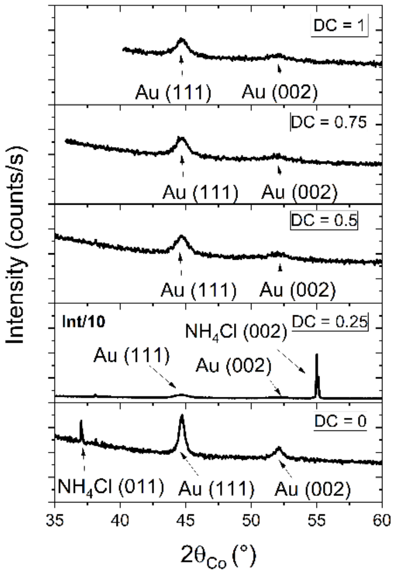

Fig. 8 XRD spectra recorded on the NC films deposited at various DC values

The patterns show that pure gold is present in the samples, regardless of the DC value. Indeed, Au(111) and Au(002) lines are systematically identified (at 44.7° and 52.1° respectively). As the duration of the HF phase increases (*i.e.* as DC increases), the intensity of these peaks decreases. Additionally, for DC = 0 and DC = 0.25, crystalline ammonium chloride is detected thanks to its typical peaks at 37.2° and 55.2°. The amplitude of the peak detected at 55.2° (for the sample deposited with a DC = 0.25) is so high that the overall intensity has been reduced by a factor of 10 to keep the same scale as the other measurements. The detection of this chloride salt is consistent with the FTIR characterization presented in section III.1.a.

From Au (111) peak broadening and using the Scherrer equation [35], the average crystallite size of the gold phase is determined and the obtained values are summarized in Table 5. It is found to be almost constant, around 7-9 nm, except in the sample produced at DC = 0 (*i.e.* LF only), but in all the cases, it remains smaller than the grain size inferred from SEM observations, meaning that the granular structures evidenced in the SEM micrographs are much more aggregates than individual gold particles.

Table 5 Determination of the average crystallite size of the gold phase

Duty cycle	**Average crystallite size**
0	18.5 ± 3.7 nm
0.25	7.5 ± 1.5 nm
0.5	9.1 ± 1.8 nm
0.75	7.5 ± 1.5 nm
1	8.7 ± 1.7 nm

III.2. SEM

The SEM images collected at low magnification (x1000) on the produced films are reported in Fig. 9. They allow visualizing the general topography of the deposits and their coverage rate.

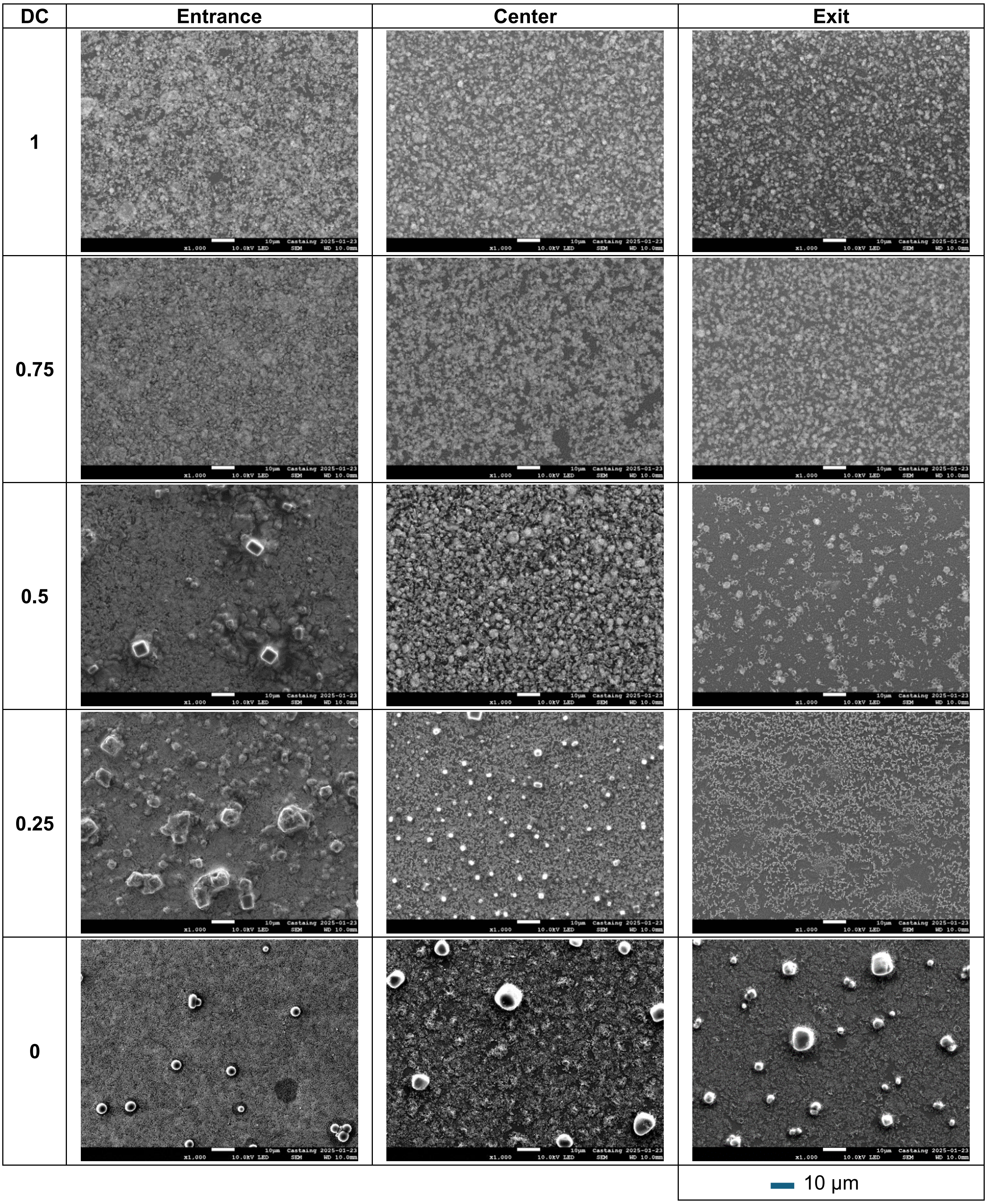

Fig. 9 SEM images obtained with the Everhart-Thornley detector at low magnification as a function of DC

First of fall, these SEM images did not exhibit localized damage on the produced films due to microdischarges.
At DC = 0.75 and 1 (mostly and only HF excitation), the distribution of NPs is much more uniform over the glass substrate surface, with an almost total and dense coverage.
At DC = 0.5, large, faceted crystals are present at the entrance of the sample. They seem to “melt” under electron beam irradiation and have various shapes. For the other positions, no crystals are observed. However, a decrease in the density of gold NPs on the substrate is noticeable. They are found to aggregate in clusters at the exit of the discharge region.
At DC = 0.25 (mostly LF), similar crystals are present at the entrance and the center of the sample. They too are unstable under electron beam irradiation. At the exit, no crystals are observed. A decrease in the density of gold NPs on the substrate is also noticed.
At DC = 0 (only LF excitation), the images show that there is a dense deposition and a very thin matrix at the entrance. The amount of NPs seems to be lower at the exit as already suggested by UV-Vis absorption spectroscopy (Fig. 4 in section III.2). Similar crystals are also found, regardless of the position on the substrate.

EDS spectra are also collected on all the samples at the different three positions. The obtained weight percentage on the checked elements, focusing on the large observed crystals, at DC = 0, 0.25 and 0.5, are consistent with the presence of NH_4Cl , in agreement with former FTIR (Fig. 5 and Table 3 in section III.1.a) and XRD (Fig. 8 in section III.1.c). analyses. A representative EDS spectrum is given in Fig. 10 to illustrate such a purpose.

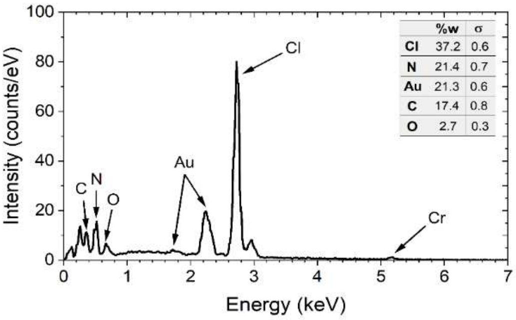

	%w	σ
Cl	37.2	0.6
N	21.4	0.7
Au	21.3	0.6
C	17.4	0.8
O	2.7	0.3

Fig. 10 Representative EDS spectrum acquired on a crystal obtained at low DC

The weight percentage obtained by EDS measurements exhibits that crystals are mainly composed of nitrogen and chlorine. These crystals may correspond to a salt such as NH_4Cl which has been identified for these samples thanks to FTIR analyses (Fig. 5 and Table 3 in section III.1.a) and XRD analyses (Fig. 8 in section III.1.c).

Another set of images was taken with a magnification of 10000 (Fig. 11), emphasizing atomic number contrast, also known as compositional contrast.

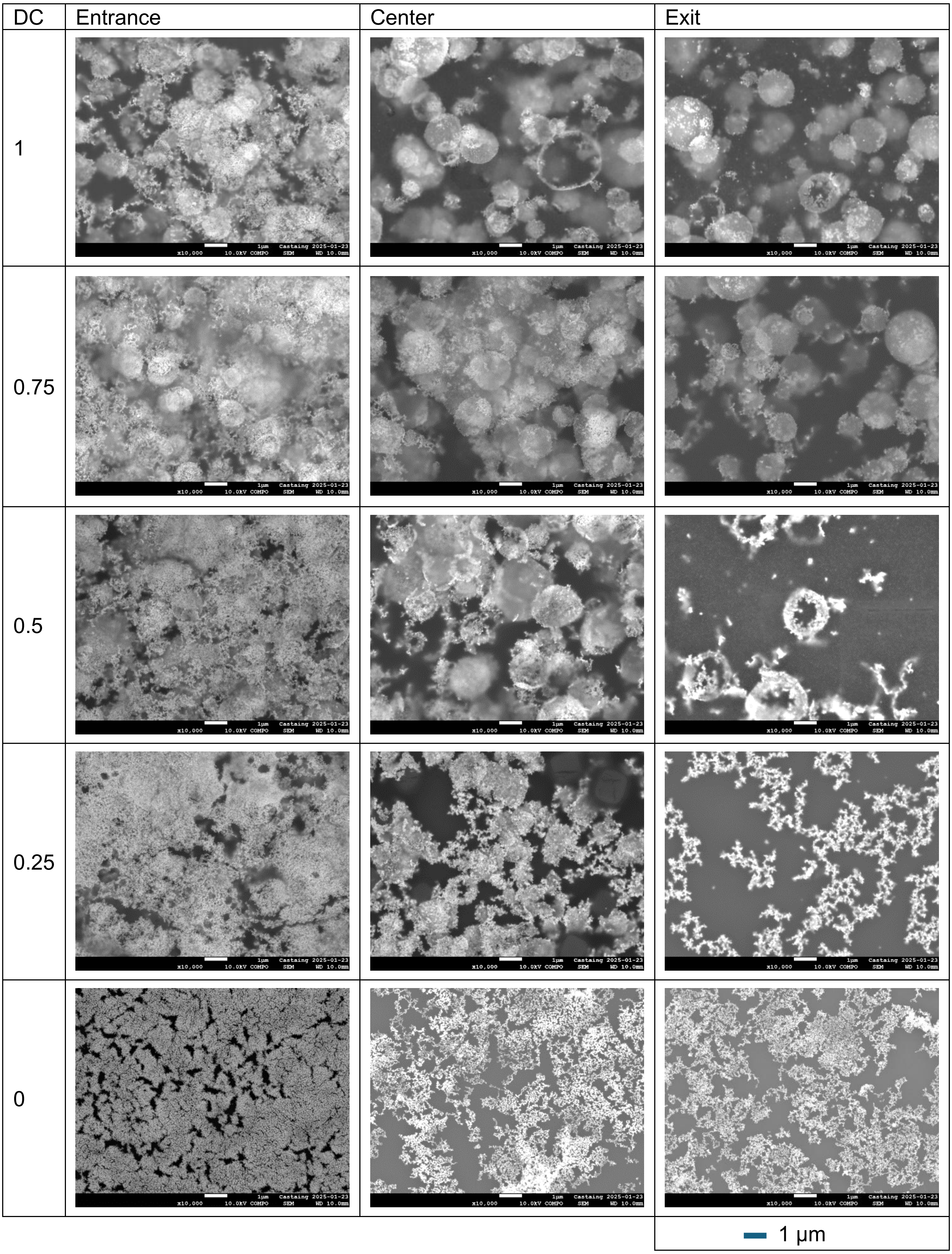

Fig. 11 SEM images obtained with a backscattered electrons detector at the entrance, center and exit position of the produced films at different DC values

The images show a better uniformity of gold NPs distribution for high DC values (DC > 0.5). This is due to the fact that, within these conditions, particles have more time to cross the gas gap before the next deposition phase.

Gold NPs density in the films prepared at low DC values (DC < 0.5) is high only at the entrance positions.

Particles appear to be agglomerated, whatever DC value, but the type of agglomeration differs according to the experimental conditions. For long low-frequency durations, the particles are assembled in the form of chains or grape clusters (DC = 0 and DC = 0.25), whereas for short ones (DC ≥ 0.5), the agglomerates have a disk-like appearance. This specific shape raises the question of NC film synthesis through the deposition and subsequent evaporation of droplets on the surface. Indeed, all these circular domains are a few microns in diameter, which may correspond to the size of a droplet.

III.3. Discussion

The formation of NC films by dual-frequency discharges relies on a compromise between metal precursor reduction, organic matrix growth, NPs transport, and solvent evaporation dynamics. As reported in the literature [16], HF excitation should enable efficient reduction of metal salts, leading to a higher proportion of reduced gold, and enhance matrix polymerization, which results in dense in-particle and thick deposits. However, this study shows that applying an HF phase for too long time may induce a rapid matrix growth, which can trap the gold salt within the polymer before a complete reduction. This leads to partially reduced gold cations precipitated as salts and embedded in the organic matrix of the deposits, as shown by XPS results (Fig. 6). Conversely, previous work showed that LF excitation promotes a more gradual structuring of the matrix, but proves an uncomplete reduction of the gold salt, resulting in the presence of partially or totally oxidized gold. However, in this study, a complete Au reduction seems to occur only when the LF proportion is high, *i.e.* for low DC values (Fig. 6). However, considering that under these conditions the organic matrix growth rate is expected to be low, it seems reasonable that Au reduction occurs both in the gas phase and at the surface. At low energy (*i.e.* at lower DC values), the formation of by-products such as ammonium chloride (NH_4Cl) is observed. Literature only report the formation of this salt via unwanted reactions in boron nitride synthesis processes [36]. The presence of ammonium chloride could be responsible of the increase of the viscosity of the deposits, which in turn could induce the observed blueshift in the UV-Visible plasmonic band (as shown in Fig. 4). Reversely, at high energy (*i.e.* at higher DC values) NH_4Cl is not or less present, not detected by XRD, and the produced deposits are denser and thicker.

The gold crystallite size does not seem to be affected by the applied DC value. It remains almost constant, between 7 and 9 nm for all investigated values. Only the DC = 0 condition exhibits a significantly larger size (close to 20 nm), which can be attributed to different reduction mechanisms in the absence of the HF phase. This weak dependency to DC must be highlighted because it differs from what was reported in the literature. Indeed, Nadal *et al.* observed a crystallites size decrease by increasing the DC value. They assume that the increase of NP growth time leads to larger NPs which are too heavy to reach the surface in time during the phase [16].

According to SEM observations, gold NPs, but their spatial organization depends on the DC value. By increasing the DC value, specific circular domains (such as disk-like structure) are formed, reasonably due to the deposition and evaporation of liquid microdroplets onto the substrate surface. These deposited droplets contain either unreacted gold salt and/or metal

NPs. They leave circular residues upon drying. In some cases, a coffee-ring–like structure can also be observed, where particles accumulate preferentially at the perimeter of the droplet due to capillary-driven outward flows during solvent evaporation [37, 38].

In former investigations, the influence of DC on the produced NC films was seldom studied. Perdrau *et al.* [18] for instance, focused on DC = 0.25 only. For this value, they observed similar plasmonic properties and almost the same chemical compositions obtained in our work, if one excepts the presence of ammonium chloride. Nadal *et al* [16] reported results on the influence of the DC variation at lower gold salt concentration (C = 0.025 wt% Au) and confirmed that better NPs surface coverage can be obtained for high DC values. However, they did not investigate the influence of the DC on the chemical composition of the NC thin films as well as on gold reduction. Brunet *et al* [39] also reported the same conclusions on the influence of DC on the morphological NC film characteristics, even if they were operating with colloidal TiO_2 solution. The consistency of these former results with our and their conclusions are consistent with our morphological NC film analysis.

The mechanisms for our plasma gold salt reduction process is supposed to be similar to those already described in previous deposition processes. Free plasma electrons, and probably in-situ formed reactive species, such as OH radicals, too, are involved in the reaction [18, 40, 41]. However, the mechanisms of organic matrix growth seem to be different, since the NPs-containing circular domains, observed here within the organic layer, have not been reported in the previous works operating with Ar carrier gas. For NC thin film deposition in N_2 DBD, the higher discharge energy could result in a stronger plasma/aerosol interaction and increased heating of the sample surface, which in turn may promote distinct growth dynamics and thus account for the observed differences.

IV. Conclusion

This study highlights that the investigated synthesis process, which combines a plasma process with an aerosol of gold salt alcoholic solution in N_2-DBD, enables the deposition of NC thin films, based on a polymer matrix embedding gold NPs. In practice, gold salts are injected that are likely reduced into metallic NPs by free plasma electrons and also by radicals resulting from the dissociation of the polymer matrix precursors, here isopropanol.

The results show that the distribution of NPs in the NC films is directly related to the duration of the HF excitation phase. In fact, the higher the DC, the better the distribution of these NPs along the sample surface. For DC ≥ 0.5, it is possible to observe disk-like structures filled with NPs. This morphology likely results from the drying of liquid microdroplets containing unreacted gold salt or plasma-synthesized Au nanocrystals, which leave circular residues. At high DC, also thick and dense organic matrix growth is promoted. In contrast, at low DC, the produced layers are chemically less stable and more viscous, *i.e.* at low energy applied per precursor molecule. This low energy promotes the formation of dissociation by-products such as ammonium chloride.

The optimal deposition condition for moderate matrix growth and good gold NP distribution is therefore a DC value of 0.75. Further experiments need to be carried out to deepen our understanding of the mechanisms of organic matrix growth and salt reduction. For example, the influence of other deposition parameters could be explored, such as the gold concentration in the solution or the substrate temperature, the nature of the solvent, involving more carbon atoms and/or more hetero-atoms to act on the polymerization rate to limit or reversely promote the NPs encapsulation feature.

Acknowledgement

Authors would like to acknowledge the French National Research Agency for their funding of the PLASSEL Project (ANR ANR-21-CE08-0038).

Bibliography

1. Subhan A, Mourad A-HamidI (2025) Plasmonic metal nanostructures as performance enhancers in emerging solar cells: A review. Next Materials 6:100509. https://doi.org/10.1016/j.nxmate.2025.100509

2. Kumar Das P, Dhawan A (2023) Plasmonic enhancement of photovoltaic characteristics of organic solar cells by employing parabola nanostructures at the back of the solar cell. RSC Advances 13:26780–26792. https://doi.org/10.1039/D3RA03637E

3. Kaydashev V, Khlebtsov B, Kutepov M, et al (2023) Photothermal Effect and Phase Transition in VO2 Enhanced by Plasmonic Particles. Materials 16:2579. https://doi.org/10.3390/ma16072579

4. Virgili AH, Laranja DC, Malheiros PS, et al (2021) Nanocomposite film with antimicrobial activity based on gold nanoparticles, chitosan and aminopropylsilane. Surface and Coatings Technology 415:127086. https://doi.org/10.1016/j.surfcoat.2021.127086

5. Khan I, Khan I, Saeed K, et al (2023) 7 - Polymer nanocomposites: an overview. In: Ali N, Bilal M, Khan A, et al (eds) Smart Polymer Nanocomposites. Elsevier, pp 167–184

6. Uricchio A, Fanelli F (2021) Low-temperature atmospheric pressure plasma processes for the deposition of nanocomposite coatings. Processes 9:2069

7. Klages C-P, Höpfner K, Kläke N, Thyen R (2000) Surface Functionalization at Atmospheric Pressure by DBD-Based Pulsed Plasma Polymerization. Plasmas and Polymers 5:79–89. https://doi.org/10.1023/A:1009583815474

8. Sakoda T, Sung Y-M, Matsukuma K (2006) Plasma treatment on electrode surfaces of bifacial silicon solar cells. Solar Energy Materials and Solar Cells 90:1089–1097. https://doi.org/10.1016/j.solmat.2005.06.008

9. Massines F, Sarra-Bournet C, Fanelli F, et al (2012) Atmospheric pressure low temperature direct plasma technology: status and challenges for thin film deposition. Plasma Processes and Polymers 9:1041–1073

10. Fanelli F, Mastrangelo A, Fracassi F (2014) Aerosol-Assisted Atmospheric Cold Plasma Deposition and Characterization of Superhydrophobic Organic–Inorganic Nanocomposite Thin Films. Langmuir 30:857–865. https://doi.org/10.1021/la404755n

11. Becker KH (2005) Non-equilibrium air plasmas at atmospheric pressure. Institute of Physics Publishing, Bristol ; Philadelphia

12. Rane AV, Kanny K, Abitha VK, Thomas S (2018) Chapter 5 - Methods for Synthesis of Nanoparticles and Fabrication of Nanocomposites. In: Mohan Bhagyaraj S, Oluwafemi OS, Kalarikkal N, Thomas S (eds) Synthesis of Inorganic Nanomaterials. Woodhead Publishing, pp 121–139

13. Neouze M-A, Schubert U (2008) Surface Modification and Functionalization of Metal and Metal Oxide Nanoparticles by Organic Ligands. Monatsh Chem 139:183–195. https://doi.org/10.1007/s00706-007-0775-2

14. Sabzi Dizajyekan B, Jafari A, Vafaie-Sefti M, et al (2024) Preparation of stable colloidal dispersion of surface modified Fe3O4 nanoparticles for magnetic heating applications. Scientific Reports 14:1296. https://doi.org/10.1038/s41598-024-51801-5

15. Ly P-D, Ly K-N, Phan H-L, et al (2024) Recent advances in surface decoration of nanoparticles in drug delivery. Frontiers in Nanotechnology 6:. https://doi.org/10.3389/fnano.2024.1456939

16. Nadal E, Milaniak N, Glenat H, et al (2021) A new approach for synthesizing plasmonic polymer nanocomposite thin films by combining a gold salt aerosol and an atmospheric pressure low-temperature plasma. Nanotechnology 32:175601. https://doi.org/10.1088/1361-6528/abdd60

17. Brunet P, Rincón R, Martinez J-M, et al (2017) Control of composite thin film made in an Ar/isopropanol/TiO2 nanoparticles dielectric barrier discharge by the excitation frequency. Plasma Processes and Polymers 14:1700049. https://doi.org/10.1002/ppap.201700049

18. Perdrau A, Barros N, Rincón R, et al (2023) Synthesis of Gold NPs-Containing Thin Films from Metal Salt Injection in Ar or Ar–NH3 DBDs. Plasma Chemistry and Plasma Processing 43:1749–1772. https://doi.org/10.1007/s11090-023-10400-4

19. Bazinette R, Sadeghi N, Massines F (2020) Dual frequency DBD: influence of the amplitude and the frequency of applied voltages on glow, Townsend and radiofrequency DBDs. Plasma Sources Science and Technology 29:

20. Profili J, Dap S, Levasseur O, et al (2017) Interaction of atomized colloid with an ac electric field in a dielectric barrier discharge reactor used for deposition of nanocomposite coatings. Journal of Physics D: Applied Physics 50:075201. https://doi.org/10.1088/1361-6463/aa515f

21. Boissiere C, Grosso D, Chaumonnot A, et al Aerosol Route to Functional Nanostructured Inorganic and Hybrid Porous Materials. Advanced Materials 23:599–623. https://doi.org/10.1002/adma.201001410

22. Massines F, Gouda G (1998) A comparison of polypropylene-surface treatment by filamentary, homogeneous and glow discharges in helium at atmospheric pressure. Journal of Physics D: Applied Physics 31:3411. https://doi.org/10.1088/0022-3727/31/24/003

23. Lassiter JB, Aizpurua J, Hernandez LI, et al (2008) Close encounters between two nanoshells. Nano Letters 8:1212–1218. https://doi.org/10.1021/nl080271o

24. Caucheteur C (2014) Plasmons de surface : principes physiques et applications. Physique Chimie. https://doi.org/10.51257/a-v1-af3565

25. Memon AG, Channa IA, Shaikh AA, et al (2022) Citrate-Capped AuNP Fabrication, Characterization and Comparison with Commercially Produced Nanoparticles. Crystals 12:1747. https://doi.org/10.3390/cryst12121747

26. Silverstein RM, Webster FX, Kiemle D (2005) Spectrometric Identification of Organic Compounds, 7th Edition. Wiley

27. Shahravan A, Desai T, Matsoukas T (2012) Controlled manipulation of wetting characteristics of nanoparticles with dry-based plasma polymerization method. Applied Physics Letters 101:. https://doi.org/10.1063/1.4772544

28. Pajarito BB, Llorens C, Tsuzuki T (2019) Effects of ammonium chloride on the yield of carbon nanofiber aerogels derived from cellulose nanofibrils. Cellulose 26:7727–7740. https://doi.org/10.1007/s10570-019-02645-0

29. Justin Gorham (2012) NIST X-ray Photoelectron Spectroscopy Database - SRD 20

30. Casaletto MP, Longo A, Martorana A, et al (2006) XPS study of supported gold catalysts: the role of Au0 and Au+ species as active sites. Surface and Interface Analysis 38:215–218. https://doi.org/10.1002/sia.2180

31. Gold - XPS Periodic Table. https://www.thermofisher.com/fr/fr/home/materials-science/learning-center/periodic-table/transition-metal/gold.html. Accessed 16 Oct 2025

32. Bjelajac A, Phillipe A-M, Guillot J, et al (2023) Gold nanoparticles synthesis and immobilization by atmospheric pressure DBD plasma torch method. Nanoscale Advances 5:2573–2582. https://doi.org/10.1039/D3NA00007A

33. XPS Periodic Table. https://www.thermofisher.com/fr/fr/home/materials-science/learning-center/periodic-table.html. Accessed 16 Oct 2025

34. Zhao N, Fei X, Cheng X, Yang J (2017) Synthesis of silver/silver chloride/graphene oxide composite and its surface-enhanced Raman scattering activity and self-cleaning property. IOP Conference Series: Materials Science and Engineering 242:012002. https://doi.org/10.1088/1757-899X/242/1/012002

35. Tjong SC, Chen H (2004) Nanocrystalline materials and coatings. Materials Science and Engineering: R: Reports 45:1–88. https://doi.org/10.1016/j.mser.2004.07.001

36. Nehate SD, Saikumar AK, Prakash A, Sundaram KB (2020) A review of boron carbon nitride thin films and progress in nanomaterials. Materials Today Advances 8:100106. https://doi.org/10.1016/j.mtadv.2020.100106

37. Mathijssen AJTM, Lisicki M, Prakash VN, Mossige EJL (2023) Culinary fluid mechanics and other currents in food science. Reviews of Modern Physics 95:025004. https://doi.org/10.1103/RevModPhys.95.025004

38. Deegan RD, Bakajin O, Dupont TF, et al (1997) Capillary flow as the cause of ring stains from dried liquid drops. Nature 389:827–829. https://doi.org/10.1038/39827

39. Brunet P, Rincón R, Matouk Z, et al (2018) Tailored Waveform of Dielectric Barrier Discharge to Control Composite Thin Film Morphology. Langmuir 34:1865–1872. https://doi.org/10.1021/acs.langmuir.7b03563

40. Vasudevan A, Shvalya V, Košiček M, et al (2022) From faceted nanoparticles to nanostructured thin film by plasma-jet redox reaction of ionic gold. Journal of Alloys and Compounds 928:167155. https://doi.org/10.1016/j.jallcom.2022.167155

41. Nitta K, Shimizu Y, Terashima K, Ito T (2021) Plasma-assisted synthesis of size-controlled monodisperse submicron gold particles using inkjet droplets. Journal of Physics D: Applied Physics 54:33LT01. https://doi.org/10.1088/1361-6463/ac02f8